μ-FTIR mapping: Distribution of impurities in different types of diamond growth

D. Howell *, C.J. O'Neill, K.J. Grant, W.L. Griffin, N.J. Pearson, S.Y. O'Reilly

ARC Centre of Excellence for Core to Crust Fluid Systems (CCFS) and GEMOC, Department of Earth & Planetary Science, Macquarie University, NSW 2109, Australia

ARTICLE INFO

ABSTRACT

Developments in technology are making the application of Fourier Transform infrared (FTIR) mapping to the study of minerals more feasible. In the case of diamonds, IR spectroscopy provides a simple method of analyzing common impurities; this not only forms the basis of their classification, but may also provide insights into their age and/or thermal history. The spatial distribution of these impurities, as defined by FTIR mapping, thus can reveal significant information about the growth history of the diamond. However, this mapping technique produces thousands of spectra, creating a need for some form of automated data processing, which was previously unavailable. We describe our new computer routine, named DiaMap. It has been written to provide quantitative data on the most commonly reported IR-active impurities in natural diamonds; nitrogen concentrations and aggregation states, the intensity of the platelet (B′) band, and the presence of hydrogen. While this routine is written for application to natural diamonds, it can also be applied to synthetic diamonds. Here we demonstrate the application of the method to a natural diamond of roughly cube morphology from the Diavik mine (Canada) that contains layers of octahedral, cuboid and fibrous growth. The data show that our traditional understanding of nitrogen aggregation rates and platelet development does not apply to cuboid and fibrous diamond growth types, and lays the basis for a more intensive study of such diamonds.

© 2012 Elsevier B.V. All rights reserved.

1. Introduction

Diamonds play a vital role in understanding the nature and importance of fluid processes in the mantle [1,2]. Not only can diamonds transport samples of their growth environment as inclusions of minerals and fluids, they also can carry impurities within their structure, which provide insights into specific growth events. Infrared (IR) analysis has become a principal tool for investigating diamonds. It provides a relatively simple and rapid method for analyzing the mineral and fluid inclusions [3–7] and for identifying the most common impurities in the diamond itself, namely nitrogen (for a review of all nitrogen-based defects in diamond see [8]), hydrogen [9] and boron [10]. As a result, IR analysis has become the basis for diamond classification since the first distinction by Robertson et al. [11].

In the past, IR studies were limited to single point analyses, with linear transects of points being used to show variations in impurities across a sample [12–14]. The resolution of such transects was limited both by instrumentation, and by the labor involved in the deconvolution of many IR spectra. Since Mendelssohn and Milledge [15] first proposed the use of FTIR mapping in diamond research in 1995, developments in spectrometer and computer capabilities have been making the technique more readily available to scientists. Bench-top FTIR microscope systems are becoming more compact (reducing the time required for

an analysis) and incorporating computer controlled *x–y–z* stages (allowing automated mapping), while synchrotron radiation sources [16] and focal plane array (FPA) detectors [17,18] allow FTIR analysis on the micron scale. The generation of detailed FTIR maps results in files that contain many thousands of spectra. This has created the need for an automated process to obtain reliable, quantitative impurity data from these spectra, with minimal time requirements for the user.

While a few recent studies have shown how FTIR mapping can be applied to diamond research [19–22], they have not provided a solution to this data-processing problem. These studies either processed the data manually, or do not disclose their methods in detail nor make them freely available for others to use. Here we describe the processes performed by the new computer code DiaMap, which is the first to be fully described and made open-source. It is designed to automatically process and deconvolute IR spectra of diamonds, providing data on the spatial distribution of nitrogen impurities (both concentration and aggregation state), the presence of IR-active hydrogen, and the occurrence of platelets in natural cratonic diamonds. This code can be applied to IR spectra collected on diamonds from any instrument system, and could also be used on metamorphic and synthetic diamonds (SynDiaMap), as well as diamonds containing abundant fluid inclusions (DiaMapFluid).

We apply this new data processing technique to a sample that exhibits periods of octahedral, cuboid and fibrous diamond growth and use it to investigate the difference in impurity behavior between the different growth types. The results show that our current knowledge

---

* Corresponding author at: Tel.: +61 298504401; fax: +61 298508943.
E-mail address: daniel.howell@mq.edu.au (D. Howell).

of nitrogen aggregation rates and subsequent platelet development is not necessarily applicable to cuboid and fibrous diamond growth. This observation illustrates the type of new insights that can be obtained by this technique, and suggests both the need and the basis for a wider research program.

2. Samples and analytical techniques

The sample used in this study, DVK046N, is a natural 1.16 ct diamond cube (Fig. 1A) from the Diavik mine, Canada. A plate, 2 mm thick, was laser-cut from the original cube and the faces mechanically polished. CL imaging revealed that the diamond had a very interesting growth history (Fig. 1B). Preliminary IR mapping returned spectra saturated with respect to nitrogen, so a thinner plate (~600-μm thick) was laser cut from the original one (Fig. 1C and D). At the core of the stone is an octahedral diamond ~1 mm across, which is then surrounded by a region of transitional growth, which shows evidence of resorbed octahedral growth (Fig. 1D and G). There are also abundant fractures surrounding the octahedral core (Fig. 1E and F). After this transition, cuboid growth becomes dominant as seen by the curved, hummocky stratigraphy in the CL image (Fig. 1B, D, G and H), and this clearly changes the morphology of the diamond from octahedral to cubic. We acknowledge that natural diamonds cannot form perfect cube morphologies but we think the use of this term is preferable to confusing the use of cuboid, which solely refers to a growth type.

The cuboid growth then transitions to what we believe to be a ~0.5 mm thick layer of fibrous growth. Although this layer appears optically transparent (i.e. free from obvious inclusions) its CL image reveals no evidence of episodic growth; this characteristic is observed in fibrous diamond cubes [23]. A layer of defects, visible in the micrograph (Fig. 1E), occurs at the boundary between the cuboid and fibrous growth layers. These may have been responsible for "wetting" the already rough crystal surface [23] and creating local morphological instabilities that resulted in breaking-up of the lateral cuboid growth and creation of the columnar features of fibrous growth. After this fibrous layer, growth stratigraphy returns to the CL image of the outer layer, showing competing cuboid (curved) and octahedral (faceted) growth at the edges of the crystal (Fig. 1H). The contacts between the cuboid, fibrous and outer layers appear to be transitional as there is no evidence of resorption. The band of defects at the contact between the cuboid and fibrous layer (Fig. 1E), does not appear to be accompanied by the abundant light-scattering defects commonly associated with cuboid growth [24].

The FTIR instrument used to collect the IR maps is a Nicolet iN10 microscope, operated via Omnic Picta software. The system is purged with high-purity nitrogen gas for at least 30 min before and during the mapping to help remove any atmospheric contribution to the IR
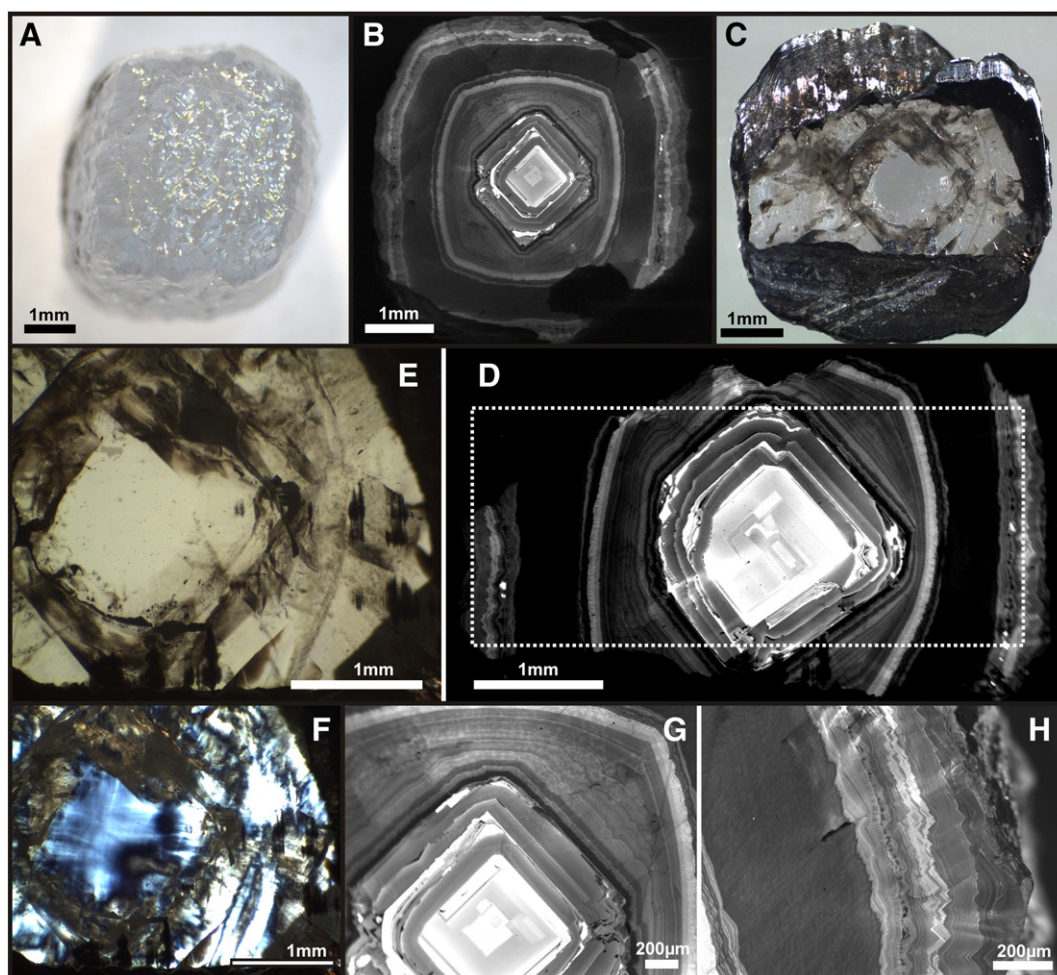

Fig. 1. Images of DVK046N. (A) A photo of the original cube morphology of the diamond. (B) CL image of the first thicker slice laser cut from the cube. (C) A photo of the second thinner slice, cut from the first one. (D) CL image of the thinner slice. The dashed white line shows the area that was FTIR-mapped. (E) Photo of the thinner diamond slice, showing the many fractures present in the stone and the absence of the light-scattering defects commonly seen in cuboid diamond growth. Note the thick layer of defects that can be seen to start at the edge of the scale bar and to trace the boundary between the cuboid and fibrous layers. (F) Same area as in (E) but taken between crossed polarizers. (G) Enlarged CL image from (B) showing the transition and possible resorption of the octahedral core. (H) Enlarged CL image from (B) showing the texture of the fibrous layer and the subsequent transition to cuboid and octahedral growth in the outer layer.

spectra. Using a $50\times50\mu m$ aperture and a liquid nitrogen-cooled MCT detector, the spectra discussed below were collected over the range of 4000 to 675 cm^{-1} with a resolution of 1 wavenumber, by 16 scans in 6 s. This short time is all that is required to obtain high-quality spectra from this FTIR system. The step size between measurement sites was the same as the aperture so that full coverage of the sample was obtained. A background spectrum, refreshed every 5 min, is used to calculate absorbance by dividing each sample spectrum and then taking the base-10 logarithm. The maps presented in the data section below contain 2880 spectra. It is important to remember that IR spectra are obtained over the entire beam path-length of the analysis. Therefore if there are sections with different characteristics within the beam path, they will be averaged out in the final spectrum.

The Omnic Picta software creates only a single data file for an area map. To obtain individual files for each spectrum this .MAP file needs to be "split". This creates an individual .SPA file for each spectrum. To obtain the spectra in .CSV (text) format, the .SPA files are run through a simple macro that inserts their x–y coordinates into the file name, in the form X145.69 Y-1489.10. CSV.

3. Data processing methodology

Fig. 2 shows the IR spectrum that is intrinsic to diamond (i.e. Type IIa), with the main feature occurring between 1800 and 2700 cm^{-1}. It also shows the nitrogen-related features that occur in the region of 1000–1400 cm^{-1}. There are three features in addition to the intrinsic diamond and nitrogen features that are of interest in this study. The first is the B′ band that is the result of platelets. It occurs within the region of 1358–1378 cm^{-1}. The second is an additional feature that the platelets create as a result of their lattice vibrational mode, known as the D component [25]. It occurs in the region 1140–1340 cm^{-1}, which overlaps with the nitrogen features. The third feature relates to the vibrations of hydrogen. The main band (shown in Fig. 2) occurs at 3107 cm^{-1} with a subsidiary band at 1405 cm^{-1} [9]. Numerous significantly smaller bands have been reported in the region between 2786 and 3394 cm^{-1} and have also been attributed to hydrogen. Due to its rarity, any spectral contribution related to boron (2700–3000 cm^{-1}; [10,26]) is not dealt with in this study.

A description of the processes performed by DiaMap is given below. It is based upon the CAXBD97.xls spreadsheet produced by Dr. David Fisher (DTC Research Centre, Maidenhead), which utilizes a least-squares-fitting approach to the deconvolution. In simple terms, it involves scaling and combining between one and three reference spectra to fit the raw data. However, there are several key differences between the two techniques. Firstly, DiaMap does not require the spectra to be baseline-corrected or normalized, nor to have a Type IIa spectrum

Fig. 2. An illustration showing the characteristic IR features of diamond. The main spectrum shows the intrinsic absorption of Type IIa (nitrogen-free) diamond. Inset are the features related to the individual nitrogen centers as well as the platelet (B′) band, D component and hydrogen band.

subtracted from it prior to the deconvolution. These important steps are carried out within the routine. Secondly, the fit of the individual nitrogen components is only carried out between 1000 and 1350 cm^{-1}, instead of up to 1400 cm^{-1}, to prevent any large B′ band having an effect on the fitting process. Thirdly, DiaMap provides additional impurity data; the presence of both platelets and IR-active hydrogen. DiaMapFluid can also provide data on the peak heights of the OH and carbonate bands (using the methodology of Navon et al. [3]) when applied to the study of fluid-inclusion-bearing diamonds. Finally, the code is automated to process thousands of spectra at a time, and provides the data as a simple text output file that easily can be used to plot the results using their spatial context.

3.1. Coding components and preliminary processes

The DiaMap routines have been written in the PERL programming language. They use a downhill simplex minimization function, Amoeba (first described by Nelder and Mead [27]), to find the best fit in our normalization and deconvolution process. The routines we use are taken directly from the CPAN libraries [28]. We have incorporated them into the code; thus the code does not require additional software to be installed so that it can function.

DiaMap creates a list of all the *.csv or *. CSV files in the working directory and loops through them sequentially, extracting their impurity data on each pass. The code also extracts the x and y coordinates from the file title to be used in the final output. In the case where the .csv files do not have x and y coordinates as their title, the code will simply take each file name and place that in the x coordinate column of the output.

The reference spectra used for the deconvolution are contained within the scripts. The five arrays, C, A, and N$^+$ (SynDiaMap), and A, B and D (DiaMap) are implemented over the region of 1000–1350 cm^{-1}, and refer to the four documented nitrogen contributions (C center [29]; A center [30]; X or N$^+$ center [31]; B center [32]) and the platelet contribution (D component [25]). A Type IIa reference spectrum is used over the range 675–3999 cm^{-1}. The raw data, imported from the individual spectral files, are interpolated so that they have the same single wavenumber spacing as the reference spectra.

3.2. Normalization

For known calibrations of the nitrogen components to be applied to the diamond IR spectrum, it first needs to be normalized to a known sample thickness. This also requires conversion of the y-data component from absorbance to absorption coefficient [15]. To do this, DiaMap first attempts to fit the interpolated raw data to the Type IIa reference spectrum. This is carried out over the spectral region of 1800–2670 cm^{-1}, using a least-squares-fitting approach combined with a basic linear correction (or baseline) to the raw data. The region between 2313 and 2390 cm^{-1} is excluded from this fit, simply to minimize any errors that might be introduced by a large atmospheric CO_2 component. Once this fit is achieved, the minimum value in the region of 1990 to 1995 cm^{-1} (A_x) is found and then used to calculate the conversion factor (F);

$$F = 11.94/A_x \tag{1}$$

All of the absorbance (y) values can then be multiplied by this conversion factor, to obtain the spectrum in units of absorption coefficient. Finally, the fitted Type IIa spectrum is subtracted from the raw data to remove any tail of the intrinsic diamond absorption from the nitrogen-dominated region.
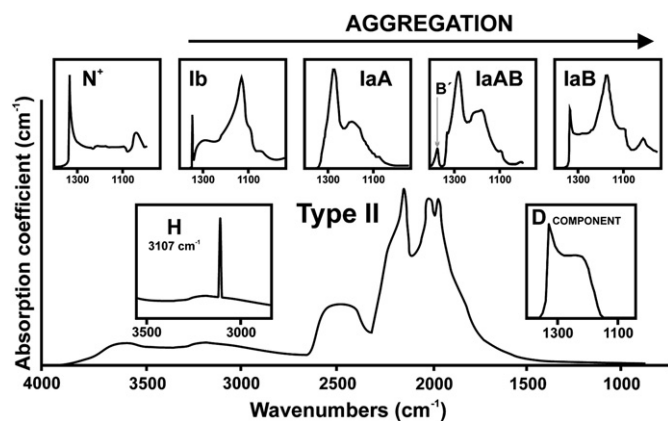
3.3. Spectral deconvolution

Over the range of 1001–1350 cm^{-1}, the individual nitrogen components (see Fig. 2) are fitted to the raw data. This is again performed using a least-squares fit combined with a new linear correction (baseline) of the raw data. To reduce the degrees of freedom within this calculation, only three reference spectra are ever used together. Due to the antiquity of many natural cratonic diamonds, DiaMap uses the A, B and D components to deconvolute their spectra. For metamorphic and synthetic diamonds, the C, N$^+$ and A components are used in SynDiaMap. For the focus of this study, i.e. natural cratonic diamonds, the fitting of the A, B and D components is based upon the following constraints:

– no component can have a negative value
– only a spectrum that contains a B component can contain a D component.

The quality of the fit is measured by providing a value for the sum of the squares (i.e. the difference between each individual data point and the fitted point, squared and summed together). Concentrations are then determined for the various components using the values of the absorption coefficient at specific wavenumber positions. An absorption coefficient value of 1 cm^{-1} is produced at:

– 1130 cm^{-1} by 25±2 ppm C centers [29]
– 1332 cm^{-1} by 5.5±1 ppm N$^+$ centers [31]
– 1282 cm^{-1} by 16.5±1 ppm A centers [30]
– 1282 cm^{-1} by 79.4±8 ppm B centers [32].

The D component, related to the platelet defects, also contributes to the total absorption at 1282 cm^{-1}. The D component used in the deconvolution of this study is defined in the appendix of Woods [25]. No actual restrictions on the D component are implemented in this deconvolution routine, but a check of the relationship between the I(B′) and D components proposed by Woods [25] can be performed to see if the values are in keeping with what should be expected. While DiaMap does not take into account any other absorption features that may occur in the one-phonon region, the open-source nature of the code allow users to add any features they like to the deconvolution routine.

3.4. Other impurities

DiaMap also provides data on the platelet and IR-active hydrogen-related features. For platelets it calculates the integrated strength, I(B′) of the B′ band, as well as its position and maximum height. To do this, a third-order polynomial baseline is fitted to points either side of the B′ band, namely 1350–1356 cm^{-1} and 1416–1430 cm^{-1}. This baseline is commonly close to being linear but can occasionally be curved. Then another third-order polynomial is fitted to data in the ranges 1380–1394 cm^{-1} and 1416–1430 cm^{-1}. This is in case the B′ band is very broad (i.e. has a tail extending to wavenumbers greater than 1400 cm^{-1}) and may be affected by the occurrence of the secondary hydrogen band at 1405 cm^{-1}. Treating each data point as a column with a width of 1 cm^{-1} and multiplying it by its height gives an area value for each point. The total sum of the area can then be obtained. Between 1350 and 1379 cm^{-1}, the area is that which lies below the data but above the baseline, while between 1380 and 1420 cm^{-1} the area is that which lies below the polynomial fit to the data and above the baseline (Fig. 3). The peak height is obtained by calculating the maximum value in this region, and the corresponding wavenumber represents the peak's position. The height of any secondary hydrogen band that might be present is calculated by subtracting the polynomial data curve from the raw data at 1405 cm^{-1}.

The primary hydrogen band is at 3107 cm^{-1} and is measured by its height. As it occurs outside the region of any previous baseline
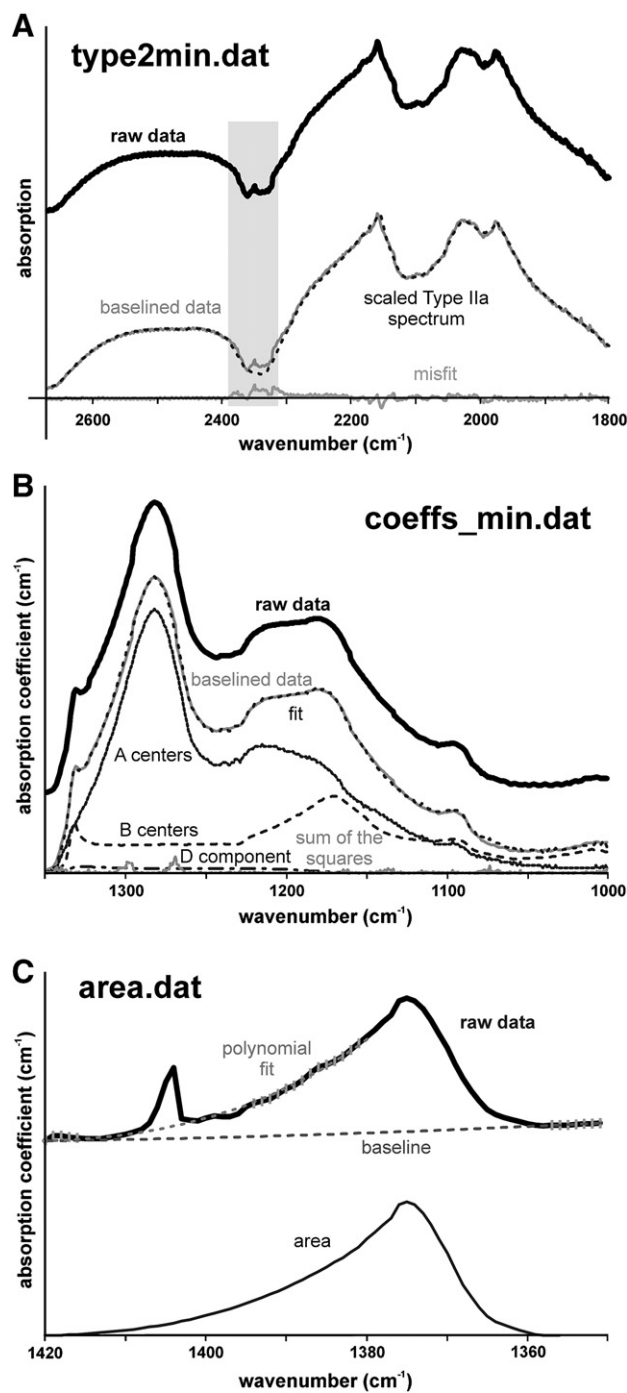

Fig. 3. Plots produced from the three additional output files generated by the DiaMap routine. (A) The quality of the fit to the Type IIa spectrum (type2min.dat). Note the light grey area between 2313 and 2390 cm^{-1} is omitted from the sum of the squares fitting as it can be seen to be the largest region of misfit. It is due to atmospheric CO_2. (B) The various components used in the deconvolution to obtain nitrogen concentrations and aggregation states (coeffs_min.dat). (C) The data, baseline and polynomial fit to the data used to calculate the intensity of the platelet band (I(B′); area.dat). The small grey ticks represent the points to which the baseline and the polynomial are fitted.

correction, and since it falls within the region of broad OH-related features (2800–3700 cm^{-1}), it is important to subtract a background value from this peak. The hydrogen peak height is calculated by finding the maximum value in the range 3106.5–3107.5 cm^{-1}. The background value is taken as the average of two points, one on either side of the H peak (using the regions 3096.5–3097.5 cm^{-1} and 3116.5–3117.5 cm^{-1}).

The data obtained from diamonds that contain abundant fluid inclusions, using DiaMapFluid, relate to the band heights of both the water (OH) and carbonate contributions. Using the interpolated raw data from which a Type IIa spectrum has been subtracted, we need to apply new baseline corrections to the areas of interest. For the water band, a polynomial baseline is fitted to the data over the regions 3900–3980 cm^{-1} and 2600–2750 cm^{-1}, while for the carbonate band the regions are 1800–1950 cm^{-1} and 1350–1357 cm^{-1}. Then the peak heights at 3420 cm^{-1} (water) and 1448 cm^{-1} (carbonate) are calculated once the baseline correction has been applied. To convert the band heights to concentrations, the method of Navon et al. [3] is applied. Therefore the DiaMapFluid code can output the concentration of both water and carbonate (in terms of CO_2) in ppm, and the water/carbonate ratio.

3.5. Outputs

DiaMap exports its main outputs to both the screen and an output file (called output.dat). The format of the output file is ASCII; it contains a row of data for each spectrum, with columns in the following order; (1) the x coordinate (X), (2) the y coordinate (Y), (3) the nitrogen concentration in the form of A centers (Na), (4) the nitrogen concentration in the form of B centers (Nb), (5) the contribution of the D component (Nd), (6) the total nitrogen concentration, i.e. $Na + Nb$ (N_total), (7) the percentage of B centers i.e. $(Nb/N\_total) \times 100$ (Na_Nb %), (8) the sum of the squares from the nitrogen deconvolution fit (sum_squares), (9) the height of the hydrogen band at 3107 cm^{-1} (H), (10) the area of the B′ band (area), (11) the peak position of the B′ band (corresponding wavenumer), (12) the height of the B′ band (Biggest in 1351–1380 range), and (13) the height of the hydrogen band at 1405 cm^{-1} (1405 peak).

In conjunction with this standard output, three other files are created by DiaMap; type2min.dat, coeffs_min.dat and area.dat. These data files are recreated with each input file. The file type2min.dat contains information from the Type IIa spectrum fit, presented in the following columns: wavenumber, original data, Type IIa spectrum, the fitted real data, the scaled Type IIa spectrum, and the misfit (Fig. 3A). The file coeffs_min.dat contains information on the deconvolution and contains the columns: wavenumber, the real data, the a, b, and d components, the fitted spectrum (i.e. $aA + bB + cD$), the baselined data, and the square of the misfit between them (Fig. 3B). The area.dat file contains information from the calculation of the B′ band: wavenumber, original data, the baseline polynomial, the third-order data-fitting polynomial, and the area of the data (at that wavenumber, i.e. data–baseline, or polynomial–baseline, depending on wavenumber; Fig. 3C). These files are overwritten with each new input file.

SynDiaMap creates a similar output file to DiaMap, except that the nitrogen components are changed to Nc, Na and Nx. As no area calculation is performed, data for the area, position and height of the B′ band are omitted from the output file. Two of the three additional output files are also created; type2min.dat and coeffs_min.dat, with the C, A and N+nitrogen components being provided in the latter file. Along with the x–y coordinates of the spectrum, the DiaMapFluid output file contains the heights of the water band (at 3420 cm^{-1}) and carbonate band (at 1448 cm^{-1}) above their respective baselines. It then provides the concentrations of each component in ppm and then finally provides the molar water/carbonate ratio. Two additional output files, OHband.dat and CARBband.dat, are also generated. They contain data in the following columns; wavenumber, the real data, baselined data.

3.6. Errors and uncertainties

This approach for the deconvolution of IR spectra of diamond is thought to provide nitrogen concentrations that are accurate within

±10% [33]. When data processed by both the DiaMap and CAXBD97.xls methods (see supplementary material) are compared, it is clear that our DiaMap routine does not make this uncertainty any worse. The nitrogen concentrations, and subsequently calculated aggregation states, from the two methods are always within the 10% uncertainty of one another. The standardization of many of the processes involved in the deconvolution, which commonly are performed manually and can vary significantly (e.g. baselining), makes the data obtained using DiaMap very reproducible.

The standardization of the calculation of I(B′) is complicated due to the variable position and form of the B′ band, combined with the fitting of a baseline and polynomial to eradicate any contribution from the 1405 cm^{-1} hydrogen band. The data in the supplementary material suggest that errors of up to 35 cm^{-2} can occur when there are no real platelet features to measure. This will be due to noise and the large region that is being included. For larger platelet bands, i.e. >50 cm^{-2}, the uncertainty is <20 cm^{-2}, while the uncertainty in both the position and height of the band is 1 cm^{-1}.

While the calculation of the height of the primary hydrogen band (3107 cm^{-1}) is relatively simple, the secondary band (1405 cm^{-1}) is complicated by both the platelet and carbonate contributions. However, values of >1 cm^{-1} are deemed significant for both features, and the uncertainty in the primary feature is <3 cm^{-1}. The method of obtaining water and carbonate concentrations [3] is believed to be accurate to ~30%. It is important to point out that the spectral quality of analyses carried out on diamonds containing abundant fluid inclusions is often impaired by light-scattering, and this can have a knock-on effect to the quality of the fit for the nitrogen data. The carbonate features can also significantly affect the calculation of the platelet area. Ultimately, as with any automated data processing technique, we advise scrutiny by the user to check that nothing untoward is occurring. But with typical diamond IR spectra, DiaMap offers a rapid, accurate and automated method of processing large quantities of data with minimal effort on the part of the user.

4. Results

The results of the IR mapping are shown in Fig. 4. It is clear that different components highlight different parts of the diamond's growth stratigraphy. For example, the octahedral core shows the most aggregation of nitrogen from A centers to B centers, and consequently has the highest platelet intensity in the stone. The inner and outer cuboid layers show no detectable B centers at all, and low hydrogen intensities compared to the octahedral and fibrous layers. The fibrous layer has the highest nitrogen concentrations in the stone, with low levels of aggregation to IaB (5–10%), and high intensities of the main hydrogen band. These characteristics are also shown in a transect across the IR map (Fig. 5). A regularity plot (I(B′) vs μ$_B$, after [25]) and an isochron plot (nitrogen concentration vs %IaB after [34]) of the data from the three main growth layers are shown in Fig. 6. One very important point to make is that the IR spectra collected from the fibrous layer of DVK046N show no evidence of fluid or mineral inclusions being contained within it. This is supported by its transparent appearance (Fig. 1C and E).

5. Discussion

Several interesting impurity characteristics of DVK046N are revealed by the IR mapping. The first is that the fibrous layer shows low levels of nitrogen aggregation (5–10% IaB), while the older cuboid layer it surrounds shows no formation of B centers at all. It is hard to know whether this is simply the result of the increased nitrogen concentration of the fibrous layer (1700 ppm compared to 900 ppm in the cuboid layer), or the result of aggregation in the cuboid layer being retarded. Rondeau et al. [35] proposed that the presence of abundant hydrogen in cuboid diamond, with H residing
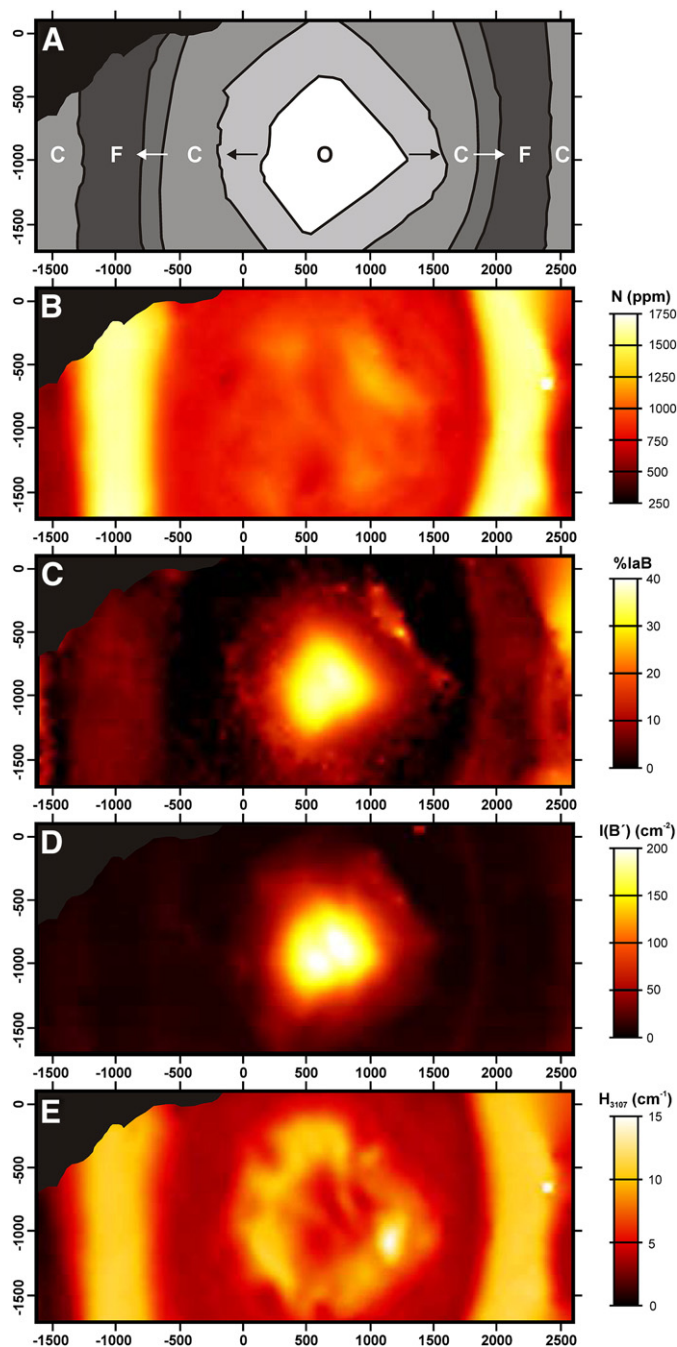
Fig. 4. Impurity maps obtained from the 2880 spectra that make up the FTIR map (scale in microns). (A) A schematic sketch of the growth layers based upon the CL image (Fig. 1D). O = octahedral growth, C = cuboid growth, F = fibrous growth, arrows represent transitional growth. (B) Map of total nitrogen concentration (ppm). (C) Map of nitrogen aggregation states (%IaB). (D) Map of the integrated area of the B′ platelet band (cm^{-2}). (E) Map of the maximum height of the 3107 cm^{-1} hydrogen related band (cm^{-1}). Plots were produced using GMT software [43].

specifically at the A centers, prevented formation of B centers from taking place. However, more recent IR mapping of a diamond containing volumes of mixed-habit growth [36] has shown that the concentration-adjusted rate of nitrogen aggregation was the same in the cuboid sectors as in the octahedral ones. If the data from the cuboid and fibrous layer of DVK046N were to fall on the same isochron (i.e. they are of similar age and have experienced the same thermal history; Fig. 6) then the cuboid layer would be expected to contain at least a few percent of B centers.

These data obviously raise questions about the rate of nitrogen aggregation in fibrous and cuboid diamond growth. Boyd et al. [13] made an interesting point regarding the aggregation rates of nitrogen in fibrous and cuboid diamond. The issue relates to the fact that nitrogen activation energies and subsequent aggregation rates have been determined by experiments using high-quality octahedral diamonds. They have not been determined on poorer-quality cuboid or fibrous diamond that contains numerous defects and possible inclusions. Studies by Collins [37,38] showed that a concentration of just 5 ppm of vacancies within a diamond could enhance the rate of conversion of C centers to A centers by a factor of 50. This would undermine any attempt to interpret the age/thermal history of fibrous diamond growth based on nitrogen characteristics.

Another interesting feature of DVK046N is that despite showing low levels of B center formation, the fibrous diamond growth contains no platelet features at all. The *regular* relationship of Woods [25] (a linear relationship between the amount of nitrogen as B centers and the intensity of the platelet feature; Fig. 6) predicts that the amount of B centers measured in the fibrous growth would produce a platelet feature with intensities of ~50–100 cm^{-2} in a regular diamond. The fact that the data from the octahedral core fall on the regular trend show that the diamond is not irregular, as the fibrous layer cannot have experienced a heating and/or deformation event that degraded the platelets, but did not affect the octahedral core. One possible explanation of this is linked to the vacancy-enhanced aggregation process mentioned above. The conversion of A centers to B centers requires the addition of a vacancy to the four nitrogen atoms. This vacancy can be obtained either by the ejection of a carbon atom that then becomes interstitial, or the incorporation of an already existing one. So not only could the vacancies present in fibrous diamond growth increase the rate of nitrogen aggregation, they may prevent the development of platelets as well. Howell et al. [36] have shown that the regular relationship of Woods [25] is not applicable to cuboid diamond growth, and the data from DVK046N suggest that this is also the case for fibrous diamond growth.

The final impurity characteristic of DVK046N that is of interest is that the cuboid layer has a much lower-intensity hydrogen band compared to the octahedral and fibrous layers. Cuboid growth is commonly characterized by a very large hydrogen band at 3107 cm^{-1} [12,35,36], sometimes with values of >60 cm^{-1}. In DVK046N, the value in the cuboid growth is on average ~3 cm^{-1}. Howell et al. [36] postulated, in accordance with the suggestion of Woods and Collins [9], that the hydrogen in cuboid diamond growth is bound to the diamond at the surfaces of *disc-crack-like* defects [24]. Such defects are commonly documented in studies of cuboid diamond growth but it is unknown whether they are intrinsic. Rondeau et al. [35] suggested the hydrogen was bound at the site of A centers and some theoretical studies have suggested this could be responsible for the 3107 cm^{-1} vibrational band [39,40]. It is important to remember that this vibrational band, which has been attributed to hydrogen, has no correlation with actual H concentrations, as the bulk of hydrogen in diamonds resides in IR-inactive forms [41].

In the case of DVK046N, there are no crack-like-disc defects in the layers of cuboid growth (Fig. 1C and E). We think this explains the lack of IR-active hydrogen. It would also suggest that these defects are not intrinsic to cuboid growth, but maybe intrinsic to cuboid growth when it occurs in conjunction with octahedral growth, i.e. mixed-habit growth. Cavities have been reported in fibrous diamond growth [42] and it is thought these would account for the IR-active hydrogen signal recorded in the fibrous growth layer. The lack of fluid inclusions within this layer would suggest that growth was not too rapid as it did not result in trapping of the fluid medium from which the diamond was growing.

6. Conclusions

Fundamental impurity characteristics of diamond have been studied in depth and form the basis of interpretation for many modern diamond
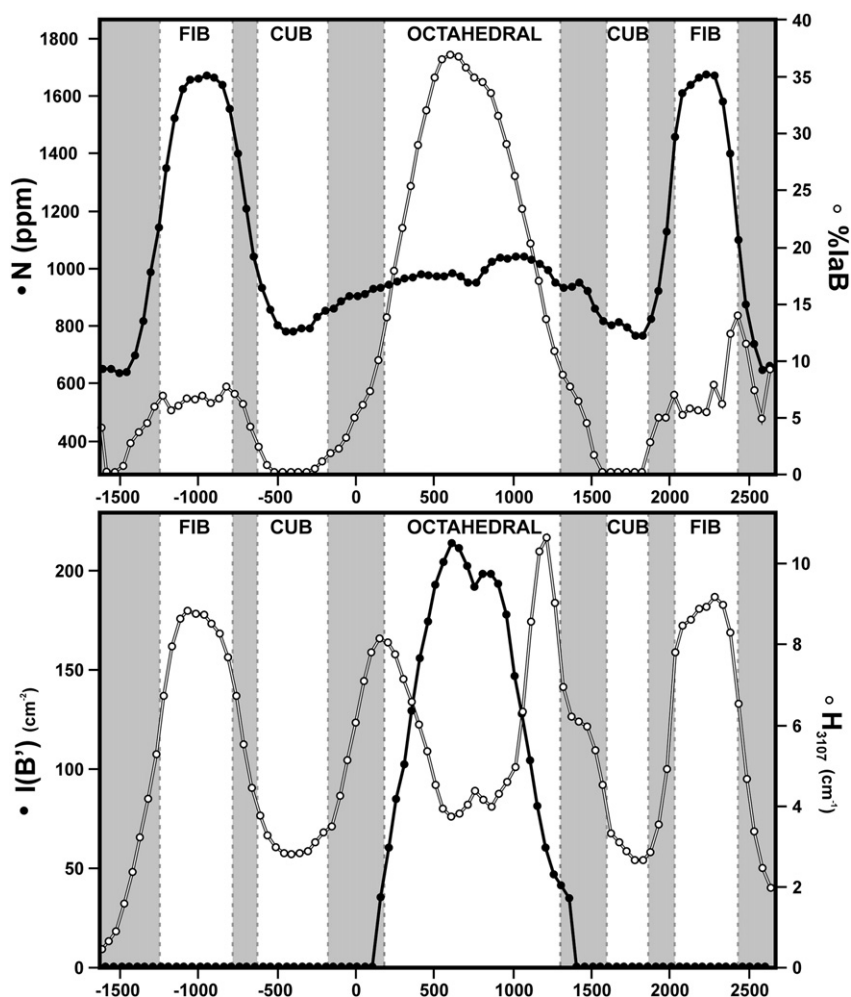
Fig. 5. Plots showing the impurity data from the FTIR mapping along a transect of y=−995 μm. The types of different growth layers are labeled (CUB = cuboid, FIB = fibrous), while the grey areas represent the transitional regions. The upper plot shows nitrogen concentration (black filled circles) and nitrogen aggregation states (white filled circles), while the lower plot shows I(B′) (black filled circles) and height of the 3107 cm^{-1} band (white filled circles).

investigations. However, the concepts of the time/temperature relationship and activation energies of nitrogen aggregation, as well as the subsequent platelet formation appear to only be truly refined for octahedral diamond growth. The data presented in this study have raised questions regarding the rate at which nitrogen aggregates in fibrous diamond, and the degree of resultant platelet formation.

To summarize the growth history of DVK046N, it is likely that the octahedral core grew significantly before, or at higher T than, the later layers. This interpretation is based on the moderate levels of nitrogen aggregation (~40% IaB) and subsequent platelet formation, as well as the possible evidence of resorption occurring before the start of the cuboid growth layer. The cuboid growth layers and the fibrous growth layer they surround appear to have grown from the same fluid, as there is no evidence of resorption between the layers. The transition to fibrous growth may have occurred for several reasons; an increase in the carbon saturation of the fluid, an increase in the concentration of impurities in the fluid, or a change in pressure, temperature or oxygen-fugacity conditions. The IR data obviously point towards impurities being the cause due to the increase of nitrogen, but carbon-isotope analysis may be able to provide insights with regard to changes in the source of the carbon. The difference in nitrogen aggregation levels between the older cuboid growth layer and the younger fibrous growth can be explained by differences in the rate at which the process occurs in the two different types of diamond. While there is debate as to whether nitrogen aggregation is retarded

in cuboid growth, the role of vacancies in increasing the aggregation rate in fibrous diamond is more conclusive [37,38]. The data therefore suggest that this second phase of growth occurred much later in the diamond's history, and that the stone then did not reside very long within the mantle prior to emplacement. This is in line with a general consensus that fibrous coats on octahedral diamond cores grow shortly before emplacement [13]. The differences in this case are that DVK046N exhibits not only fibrous growth but cuboid growth as well, and the fibrous growth does not contain abundant fluid inclusions.

This study highlights the power of IR mapping applied to the study of diamonds. The open availability of DiaMap will allow more users to easily process the large quantities of data this method can produce. However, as with any automated data processing method, scrutiny of the final output is always advised. The results of the mapping of DVK046N, when combined with our knowledge of different types of diamond growth, show that some of the models commonly used for interpreting IR data are only applicable to specific growth types. Further study of the rates of nitrogen aggregation in both cuboid and fibrous diamond are required, as well as investigation into the subsequent development of platelets. This technique opens a broad new field of research, which can provide many new insights into processes in the deep mantle.

Supplementary data to this article can be found online at http://dx.doi.org/10.1016/j.diamond.2012.06.003.
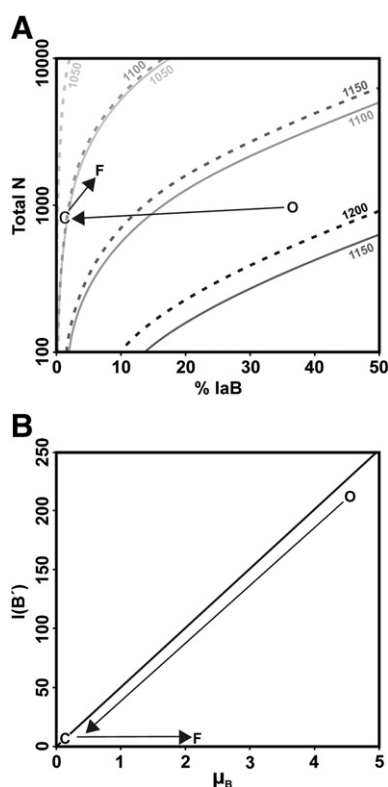
Fig. 6. (A) A plot of nitrogen aggregation *vs* nitrogen concentration, with isochrons plotted for two different residence ages (solid line = 1 Ga, dashed line = 100 Ma) and a range of mantle temperatures (in °C). (B) Regularity plot, absorbance due to B centers *vs* I(B′) (after [23]). In both plots, the use of O, C and F represents the areas where data from the octahedral, cuboid and fibrous layers plot, and the arrows represent the trend of the data as the growth layers change.

Acknowledgments

References

[1] T. Stachel, J.W. Harris, J. Phys. Condens. Matter 21 (2009) 364206, 1–10.
[2] S. Rege, W.L. Griffin, N.J. Pearson, D.P. Araujo, D.A. Zedgenizov, S.Y. O'Reilly, Lithos 118 (2010) 313–337.
[3] O. Navon, I.D. Hutcheon, G.R. Rossman, G.J. Wasserburg, Nature 335 (1988) 784–789.
[4] O. Navon, Nature 353 (1991) 746–748.
[5] E. Tomlinson, A.P. Jones, J.W. Harris, Earth Planet. Sci. Lett. 250 (2006) 581–595.
[6] O. Klein-BenDavid, E.S. Izraeli, E. Hauri, O. Navon, Geochim. Cosmochim. Acta 71 (2007) 723–744.
[7] Y. Weiss, I. Kiflawi, O. Navon, Chem. Geol. 275 (2010) 26–34.
[8] A.M. Zaitsev, Optical Properties of Diamond, first ed. Springer, Berlin, 2001.
[9] G.S. Woods, A.T. Collins, J. Phys. Chem. Solids 44 (1983) 471–475.
[10] R.M. Chrenko, Phys. Rev. B 7 (1973) 4560–4567.
[11] R. Robertson, J.J. Fox, A.E. Martin, Philos. Trans. R. Soc. Lond. A 232 (1934) 463–535.
[12] C.M. Welbourn, M.-L.T. Rooney, D.J.F. Evans, J. Cryst. Growth 94 (1989) 229–252.
[13] S.R. Boyd, C.T. Pillinger, H.J. Milledge, M.J. Mendelssohn, M. Seal, Earth Planet. Sci. Lett. 109 (1992) 633–644.
[14] D.P. Araujo, W.L. Griffin, S.Y. O'Reilly, K.J. Grant, T. Ireland, P. Holden, E. van Achterbergh, Lithos 112S (2009) 724–735.
[15] M.J. Mendelssohn, H.J. Milledge, Int. Geol. Rev. 37 (1995) 95–110.
[16] L.F. Dobrzhinetskaya, R. Wirth, H.W. Green II, Proc. Natl. Acad. Sci. 104 (2007) 9128–9132.
[17] I.W. Levin, R. Bhargava, Annu. Rev. Phys. Chem. 56 (2005) 429–474.
[18] A.A. Shiryaev, N. Johner, D.A. Zedgenizov, Acta Minerologica, Petrographica 6 (2010) 693.
[19] G.P. Bulanova, D.G. Pearson, E.H. Hauri, B.J. Griffin, Chem. Geol. 188 (2002) 105–123.
[20] Y.V. Babich, B.N. Feigelson, Inorg. Mater. 45 (2009) 616–619.
[21] Y.V. Babich, B.N. Feigelson, Geochem. Int. 47 (2009) 94–98.
[22] A.A. Shiryaev, F. Masiello, J. Hartwig, I.N. Kupriyanov, T.A. Lafford, S.V. Titkov, Y.N. Palyanov, J. Appl. Crystallogr. 44 (2011) 65–72.
[23] M. Moore, A.R. Lang, Philos. Mag. 26 (1972) 1313–1325.
[24] J.C. Walmsley, A.R. Lang, M.-L.T. Rooney, C.M. Welbourn, Philos. Mag. Lett. 55 (1987) 209–213.
[25] G.S. Woods, Proc. R. Soc. Lond. A 407 (1986) 219–238.
[26] H. Kim, M. Grimsditch, T.R. Anthony, A.K. Ramdas, S. Rodriguez, Phys. Status Solidi A 181 (2000) 51–58.
[27] J.A. Nelder, R. Mead, Comput. J. 7 (1965) 308–313.
[28] J.A.R. Williams, T. Chau, Math: Amoeba, http://search.cpan.org/~tom/Math-Amoeba-0.04/lib/Math/Amoeba.pm accessed on line 19/10/2011.
[29] I. Kiflawi, A.E. Mayer, P.M. Spear, J.A. van Wyk, G.S. Woods, Philos. Mag. B 69 (1994) 1141–1147.
[30] S.R. Boyd, I. Kiflawi, G.S. Woods, Philos. Mag. B 69 (1994) 1149–1153.
[31] S.C. Lawson, D. Fisher, D.C. Hunt, M.E. Newton, J. Phys. Condens. Matter 10 (1998) 6171–6180.
[32] S.R. Boyd, I. Kiflawi, G.S. Woods, Philos. Mag. B 72 (1995) 351–361.
[33] W.R. Taylor, D. Canil, H.J. Milledge, Geochim. Cosmochim. Acta 60 (1996) 4725–4733.
[34] T. Evans, J.W. Harris, In: in: J. Ross (Ed.), Kimberlites and related rocks, vol 2, Blackwell Scientific Publications, Melbourne, 1989, pp. 1001–1006.
[35] B. Rondeau, E. Fritsch, M. Guiraud, J.-P. Chalain, F. Notari, Diamond Relat. Mater. 13 (2004) 1658–1673.
[36] D. Howell, C.J. O'Neill, K.J. Grant, W.L. Griffin, S.Y. O'Reilly, N. J. Pearson, R.A. Stern, T Stachel, Platelet development in cuboid diamonds: insights from micro-FTIR mapping, Contrib. Min. Pet. in press.
[37] A.T. Collins, J. Phys.: Solid State Phys. 11 (1978) L417–L422.
[38] A.T. Collins, J. Phys.: Solid State Phys. 13 (1980) 2641–2650.
[39] J. Chevallier, F. Jomard, Z. Teukam, S. Koizumi, H. Kanda, Y. Sato, A. Deneuville, M. Bernard, Diamond Relat. Mater. 11 (2002) 1566–1571.
[40] J.P. Goss, C.P. Ewels, P.R. Briddon, E. Fritsch, Diamond Relat. Mater. 20 (2011) 896–901.
[41] R.J. Sweeney, V.M. Prozesky, K.S. Viljoen, S. Connell, Nucl. Instrum. Methods Phys. Res. B 158 (1999) 582–587.
[42] Y. Kamiya, A.R. Lang, Philos. Mag. 11 (1965) 347–356.
[43] P. Wessel, W.H.F. Smith, EOS Trans, AGU 72 (1991) 441.